

Deep learning-driven automated high-content dSTORM imaging with a scalable open-source toolkit

Janis T. Linke,¹ Luise Appeltshauer,² Kathrin Doppler,² and Katrin G. Heinze^{1,*}

¹Rudolf Virchow Center for Integrative and Translational Bioimaging, Julius-Maximilians-Universität Würzburg (JMU), Würzburg, Germany and ²Department of Neurology, University Hospital Würzburg, Würzburg, Germany

ABSTRACT Super-resolution microscopy offers the ability to visualize molecular structures in biological samples with unprecedented detail. However, the full potential of these techniques is often hindered by a lack of automated, user-independent workflows. Here, we present an open-source toolkit that automates dSTORM super-resolution microscopy using deep learning for segmentation and object detection. This standalone program enables reliable segmentation of diverse biomedical images, even in low-contrast samples, surpassing existing solutions. Integrated into the imaging pipeline, it rapidly processes high-content data in minutes, reducing manual labor. Demonstrated by biological examples, such as microtubules in cell culture and the β II-spectrin in nerve fibers, our approach makes super-resolution imaging faster, more robust, and easy to use, even by nonexperts. This broadens its potential applications in biomedicine, including high-throughput experimentation.

WHY IT MATTERS Super-resolution microscopy is a powerful technology that allows scientists to see the tiny structures within biological samples in incredible detail. Despite its potential, acquiring state-of-the-art super-resolved images remains challenging due to the technical expertise, time-intensive procedures, and complex analysis required. In this study, we present a scalable, open-source software toolkit that automates image acquisition by dSTORM. Leveraging deep learning for segmentation, our toolkit can accurately identify and target objects within diverse biomedical samples, even those exhibiting only low contrast. This automation significantly accelerates high-content super-resolution imaging workflows. By providing an accessible, user-friendly solution, researchers from various disciplines can harness the power of super-resolution microscopy without requiring extensive specialized training.

INTRODUCTION

In recent years many super-resolution fluorescence microscopy techniques have pushed the resolution limit to the nanometer scale, which had before been restricted to electron microscopy. Importantly, these advanced techniques retain the inherent advantages of fluorescence microscopy, which include sample preservation and target specificity, thus rendering them a valuable instrument for investigating biological phenomena with greater detail than ever before (1,2). These techniques, such as direct stochastic optical reconstruction microscopy (dSTORM) or stimulated emission depletion, have shown in numerous instances that the combination of resolution and molecular specificity holds

considerable promise for advancing scientific understanding (3,4). For example, they have allowed the first observation of the cytoskeleton in neuronal axons, showing that it is made up of rings with a subdiffractional periodicity of 190 nm, and even uncovering subtle disturbances in patients with polyneuropathy (5–7). However, they have not yet been widely applied in scientific research or even in medical routine diagnostics, due to the demand for technical expertise and knowledge (8,9).

In standard microscopy, all emissions are usually detected in a simultaneous time window, so that the optical resolution of 200 nm is the limit. In dSTORM, the enhanced resolution is achieved by temporally separating the light emission of thousands of single fluorophores, which allows the localization precision to become an order of magnitude higher. It only requires a standard wide-field fluorescence microscope and open-source software for image processing, making it in principle relatively accessible and

Submitted November 8, 2024, and accepted for publication February 26, 2025.

*Correspondence: katrin.heinze@uni-wuerzburg.de

Editor: Ulrike Endesfelder.

<https://doi.org/10.1016/j.bpr.2025.100201>

© 2025 Published by Elsevier Inc. on behalf of Biophysical Society.

This is an open access article under the CC BY-NC-ND license (<http://creativecommons.org/licenses/by-nc-nd/4.0/>).



cost-effective (10). However, the cost of achieving image resolutions of 20–50 nm includes not only a significant increase in acquisition time, extending from milliseconds to minutes, but also a limitation to a relatively small field of view (11,12), which is particularly hampering translational imaging approaches where the tissue context is key. Moreover, the temporal separation of the emissions by fluorophore blinking in dSTORM is typically achieved using strong laser illumination intensities and specialized imaging buffers, which may require expert knowledge to operate the microscope (3,13). The analysis of the high-content image data is also often a bottleneck when large biomedical images need to be divided into meaningful segments, and typically requires a high level of expertise (14) as reported on cancer cell vulnerability or histopathology studies (15–18).

Fortunately, over the last century, the application of deep learning has offered an adaptable approach to the analysis of high-content microscopy data, returning reproducible, high-quality results (19). A variety of approaches to automated segmentation for various types of images and microscopy data have been proposed in this context (19–24). While data-based adaptation of imaging regions and parameters have been published previously (25–28), these useful approaches have not found its way into the acquisition of high-content super-resolution data.

Therefore we present a user-friendly software toolkit that enhances the usability of super-resolution microscopy by integrating a deep learning model capable of segmenting diverse biomedical images directly into the image acquisition routine. Specifically, we used the trained deep neural networks (DNNs) to automatically identify suitable dSTORM imaging positions, enabling faster and more efficient imaging of content-rich biological samples containing many and/or large regions of interest to eventually maximize the number of meaningful images acquired. By using a fully trained, static model, our toolkit ensures consistent results across different users. Therefore, we demonstrate our imaging pipeline on various cellular examples and quantify the robustness of our method.

MATERIALS AND METHODS

Training and application of neural networks

Semantic image segmentation for standalone segmentation and high-throughput dSTORM was achieved using neural networks based on our previous implementation (5). All implementations for network training and data prediction were written in Python 3 using the PyTorch framework. The base network used for this work was the PyTorch implementation of DeepLabV3 with a RESNET101 backbone and random weights for initialization (29,30). The loss was calculated using cross-entropy loss and model parameters were updated using the Adam optimizer (31) with a fixed learning rate of $1e-4$ and

random model weights for initialization. `numpy`, `scikit-image`, and `matplotlib` were used for base and image operations and visualization during training (32). Jupyter notebooks with minimal input requirements are made available to facilitate use by nonexperts (33).

All models were trained on a workstation computer equipped with GPU with 24 GB memory (NVIDIA, RTX A5000, Santa Clara, CA, USA). To increase training speed, all models were trained on the GPU using the CUDA toolkit from PyTorch (30). The training was also tested on standard personal computers and cloud services.

Evaluation of the performance of the network in segmentation tasks was done using two common scores: dice score (DS, 1) for the foreground, and pixel accuracy (PA, 2) (34) for both foreground and background. Pixels were counted as foreground, if the activation of the foreground output layer was higher than the activation of the background layer. True positives (TPs) were matching positive pixels in both prediction and annotation, while true negatives (TNs) were matching negative pixels. False positives (FPs) were pixels positive only in the prediction, and false negatives (FNs) were pixels positive only in the annotation

$$DS : DS = \frac{2 * TP}{2 * TP + FP + FN} \quad (1)$$

$$PA : DS = \frac{TP + TN}{TP + FP + FN + TN} \quad (2)$$

To perform standalone segmentation of high-content microscopy images, a model and its associated settings were loaded and the model was then applied to the image in question, with the settings derived from the network training process being automatically applied.

dSTORM microscopy

Imaging was performed on a customized standard wide-field microscope (Carl Zeiss AG, Zeiss Observer Z.1, Oberkochen, Germany) and a 63× oil immersion apochromatic objective. High-power laser diodes with wavelengths of 405, 488, and 647 nm were used (TOPTICA Photonics AG, iBeam smart, Gräfeling, Germany) for fluorophore excitation in epi-fluorescence mode. Excitation intensity for wide-field and dSTORM illumination was further modulated with an optical density wheel and focused on the back aperture of the objective for uniform epi-fluorescence illumination. Emission light was then collected with an EMCCD camera (Andor, Oxford Instruments, Belfast, Northern Ireland).

For imaging experiments, the airtight samples were filled with imaging buffer containing 100 mM cysteamine hydrochloride (Sigma-Aldrich, M6500, St. Louis, MO, USA), 22 mg/mL glucose oxidase (Roth Chemie GmbH, 60281, Karlsruhe, Germany), 2 M D-glucose (Sigma-Aldrich, G7528), and 2 mg/mL catalase (Sigma-Aldrich, C1345) at pH 8.0.

Images were reconstructed either as a batch macro using the FIJI plugin ThunderSTORM (35,36), or directly in Python using the storm-analysis package, an implementation of the DAOSTORM algorithm (37,38). Image resolution was estimated using the Fourier-Ring-Correlation provided within the storm-analysis package (39).

High-throughput dSTORM with neural networks

Fully automated, high-throughput dSTORM was performed using software written in Python 3 and the microscope setup as described above. The graphical user interface was built with widgets and a live camera feed for jupyter notebook/lab (33).

For automated dSTORM imaging, the microscopy components were added to μ -Manager and controlled via the Python bridge

pycromanager (40,41). For each channel and illumination, individual configurations were created in μ -Manager (42) and then called software to separate microscopy components from the software. Camera and laser lines were controlled with pylablib (42).

First, the desired sample area was split into tiles, which were either acquired sequentially or through a continuous wide-field scan. Semantic image segmentation of these tiles was performed using neural networks trained on images from previous experiments, following the approach described earlier. Each image tile was directly fed into the network for segmentation, and—for practical reasons—the tile size used in training matched the camera's field of view. To address segmentation artifacts at tile borders, a second segmentation step was implemented. This involved creating new tiles by combining adjacent tiles and applying a center crop. Both segmentation steps and high-content imaging workflows were parallelized using multiprocessing, enabling faster object identification.

Objects and their respective dSTORM imaging positions were identified from the segmentation results using scikit-image, where non-connected foreground pixels were split into individual objects, with centroids determined as imaging positions (43). To avoid imaging the same object twice, proximity checks were performed and, whenever feasible, closely located objects were imaged within a single field of view. For objects larger than the field of view, multiple dSTORM images were acquired at random positions to ensure comprehensive sampling. Last dSTORM images were acquired at each identified position. The system supported wide-field acquisition for up to three colors independently as well as dual-color dSTORM. All imaging experiments were executed on a standard personal computer connected to the microscope equipped with 2 GB of GPU memory.

Periodicity analysis of neural axons

The periodicity of neural axons was analyzed using two methods: autocorrelation and a pairwise distance-based approach. Autocorrelation was applied to manually selected regions of interest using a custom MATLAB script (The MathWorks, Natick, MA, USA), as described previously (5). The pairwise distance method was developed in Python, utilizing the SciPy library (44). In brief, localization data of individual axons were isolated, a polynomial fit was applied, and pairwise distances were filtered based on their alignment with the fitted curve. Periodicity was then determined by correlating the distance frequencies with simulated sums of normal distributions. For benchmarking accuracy, dSTORM data sets of neural axons were generated using the SuReSim software package (45).

Testing samples

SpheroRulers

SpheroRuler samples were prepared as follows: the stock solution (Idylle, AFA-NAN-1000-647, Paris, France) was sonicated for 2 min and vortexed for 5 min. Then 2.5 μ L of the stock was diluted in 500 μ L PBS (Thermo Scientific, J67802-K2), transferred to a four-well plate (80426, Ibidi), and incubated for at least 2 h to settle on the coverslip.

CHO cells

For CHO samples, 10,000 cells (CHO-K1 ACC 110, DMSZ) were seeded in a four-well plate and grown in DMEM (Gibco, 41966) for 48 h at 37°C and 5% CO₂. Next, cells were washed, fixed in 4% paraformaldehyde in PBS for 15 min, and permeabilized for 5 min with 1% Triton-X (T8787, Sigma). Blocking was done with 500 μ L of 5% bovine serum albumin (A4503, Sigma) and 0.1% Triton-X in PBS for 30 min. Microtubules were stained with 10 μ g/mL mouse anti-beta-tubulin (T8328, Sigma). Actin filaments were labeled with

0.5 μ M Alexa Fluor 647-Phalloidin (Thermo Scientific, A22287, Waltham, MA, USA). On the following day, cells were washed three times with PBS for 5 min each and then incubated with the secondary antibodies (Alexa Fluor 647 F(ab)₂-goat anti-mouse IgG (10 μ g/mL, A-21237, Thermo Scientific). After a further three washing steps, cell nuclei were stained with Hoechst (Sigma, B2261) (1:3000) for 5 min and then washed three more times.

DRG neuron cultures

The DRGs were dissected from C57BL/6 mice at embryonic day 16 (E16) as described in (46,47). All used culture media were prepared and named as written in Appeltshauser, Junghof (47). In brief: the pregnant mice at E16 were killed by cervical dislocation, and the embryos were transferred to ice-cold L-15 medium. Under a dissection microscope, the spine was opened, and the spinal cord was carefully removed while ensuring the DRGs remained intact. Subsequently, each DRG was extracted using microforceps and transferred to ice-cold L-15 medium. Any nerve roots attached to the DRGs were removed. Subsequently, the DRGs were transferred to a sterile PDL/laminin-coated culture dish containing C-medium. After allowing them to settle for 24 h, they were incubated in NB-medium for 7 days, with medium changes performed every other day. After day 7, the medium was replaced with C-medium-containing ascorbic acid and forskolin until day 32. Finally, the cells were fixed with 4% paraformaldehyde in PBS and stored at 4°C until immunofluorescence staining was performed.

Staining of the DRG cultures followed the protocol of the CHO cells outlined above. For better staining, an additional permeabilization step for 2 h with 3% Triton-X (T8787, Sigma) and 1% bovine serum albumin (A4503, Sigma) was added after the blocking step. As the primary antibody for the cytoskeletal β 2-spectrin, a monoclonal mouse anti- β 2-spectrin antibody (5 μ g/mL, BD Biosciences, 612563, Franklin Lakes, USA) was used, and as a neuron marker a rabbit anti-neurofilament antibody (1 μ g/mL, N4142, Sigma). Alexa Fluor 647 donkey anti-mouse (715-605-150, Jackson ImmunoResearch Laboratories Inc., West Grove, PA, USA) and Alexa Fluor 488 donkey anti-rabbit IgG (7.5 μ g/mL, 711-545-152, Jackson IR) were used as secondary antibodies. DRG cultures were not stained with DAPI (Thermo Scientific) to reduce spectral overlap.

Images of teased nerve fibers and H&E sections

Training images of teased nerve fibers stained for neurofascin were published as part of a previous study, outlining sample preparation and imaging (5). Digital microscopic tissue images for nuclei segmentation and their respective annotations were retrieved from the *monnuseg* 2018 challenge (48,49).

Statistics and visualizations

All statistical tests were performed using OriginPro 2021b (OriginLab Corporation, Northampton, MA, USA). For figure creation biorender icons were used using a publishing license. Icons retrieved from: [BioRender.com/z75b986](https://www.biorender.com/z75b986).

RESULTS

We have developed a fully automated approach to super-resolution imaging (Fig. 1) that uses deep learning-based semantic segmentation to identify suitable regions directly during data acquisition. Typically, deep learning for image segmentation involves

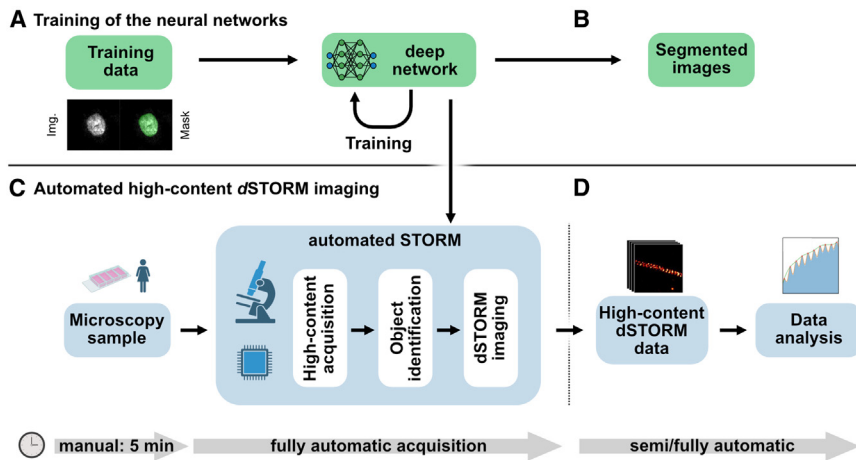


FIGURE 1 Integrating deep neural networks into dSTORM imaging. Automated STORM applies trained neural networks for the automated acquisition of super-resolution data. (A) First deep neural networks were trained on annotated (Mask) microscopy images (Img.). (B) After training the network was applied to previously unknown images as a standalone segmentation software. (C) In the second step, we used our trained networks for fully automated imaging of dSTORM. By acquiring a high-content image and segment, a map of the sample can be created for dSTORM imaging. Using this approach the user has only to be present for 5 min, and the rest can be automated. (D) As an open-source toolkit, our approach can be combined with image reconstruction and data analysis routines.

two steps: training and application of the network. In the first step, we trained the networks using labeled training data from previous microscopy images (Fig. 1 A). Here, as the second step, we implemented the network and software to be used directly for fully automated super-resolution imaging at the microscope. Thus, we present a new tool for fast, fully automated high-content dSTORM imaging (Fig. 1 C). Optionally, the trained networks, could also be used for the segmentation of various high-content image data as a stand-alone program (Fig. 1 B).

Unlike the traditional approach where a researcher selects a location, captures an image, returns, and repeats the process—potentially taking hours for just a few images—our implementation of automated dSTORM acquisition replaces manual labor with computational power (Fig. 1 C). First, the researcher places the sample on the microscope and selects a starting position. The microscope then autonomously captures a high-content image, segments it using a trained network, identifies target objects based on the segmentation, and then images these objects entirely on its own. This allowed us to spend only a few minutes at the microscope while obtaining data that would otherwise take several hours or days to collect manually. For easy application, the software was controlled with an easy-to-use graphical user interface. As a modular open-source toolkit, it was designed for easy extendibility with image reconstruction and data analysis routines (Fig. 1 D).

Training and evaluation of deep networks for segmentation of different biomedical microscopy images

To ensure high-quality automated dSTORM images, it was critical to identify target objects of interest and determine imaging positions with high precision.

Therefore, we developed an implementation of a DNN for semantic segmentation of microscopy images and evaluated its segmentation performance across various microscopy samples using common scores: DS and PA. We demonstrate successful segmentation of various biological samples: fluorescent images of CHO cells and nuclei representing cell culture, fluorescent images of nodes of Ranvier in murine nerve fibers from a specific application in a previous study (5), and hematoxylin and eosin (H&E)-stained sections of human cancer tissue as a representative nonfluorescent tissue sample (Fig. 2).

The network training for standalone image segmentation and automated super-resolution imaging was based on representative annotated samples of the bioimage data sets to be analyzed. The number of annotated objects required for successful network training varied based on the homogeneity of the objects and the sample. Due to the use of image augmentation in the training scripts, a relatively small amount of training data was sufficient. In most cases, labeling just 10–25 objects was adequate, and the annotation process took only a few minutes to complete. In cases where objects shared similar features, such as the DAPI-stained nuclei shown in Fig. 2, A–C, successful training was achieved using only a single annotated nucleus (Fig. 2 A).

While neural networks usually require thousands of training iterations to adapt effectively, our experiments showed rapid adaptation within just a few iterations, with only minimal improvements observed thereafter, as shown by high DSs within a few training iterations (Fig. 2 B). Therefore, we limited the training to fewer iterations, resulting in remarkably fast training times of just 3 min.

The network trained on just one nucleus was then applied to segment a high-content image covering nearly 2 billion pixels (Fig. 2, C and E) and achieved a pixelwise DS of 95.94%. In addition, the DNN allowed to easily retrieve metric data, such as the size

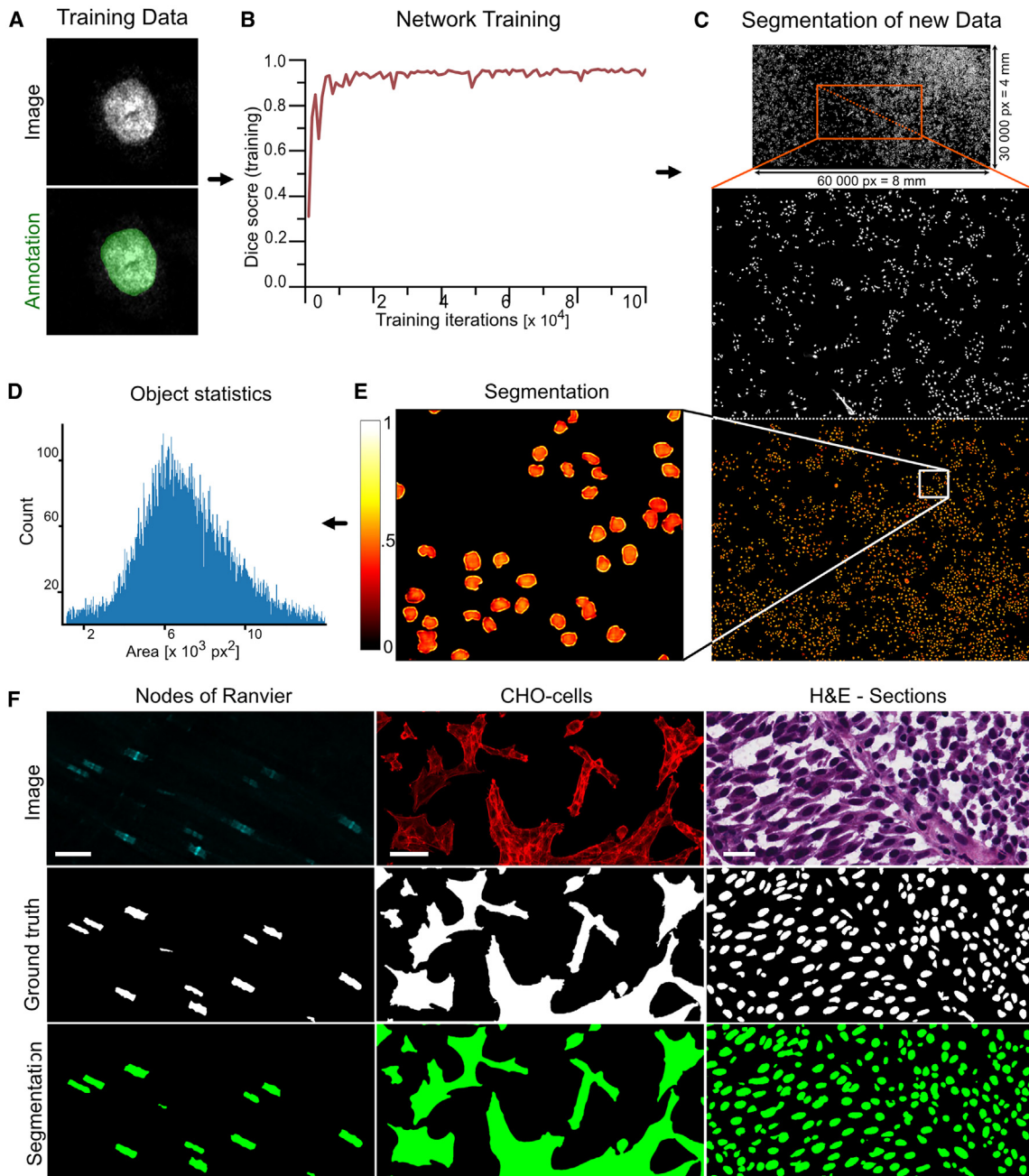


FIGURE 2 Segmentation of different microscopy images yields high-quality predictions. Deep neural networks were trained on minimal amounts of training data, reaching high DSs. (A) A singular DAPI-stained CHO cell was used for the training of the network and its annotation (green). (B) The DS on the training data increased quickly at the first iterations of the networks and later improved only marginally. (C) Application of the network on previously unknown data allowed segmentation of large high-content image data of DAPI-stained nuclei. (D) In addition to recognition, DNNs allow us to easily retrieve metric data, such as the size distribution of $n = 14,281$ nuclei detected within the image in (C). (E) Segmentation of nuclei (orange, nucleus; black, background). Intensity is scaled based on the network's confidence that the pixel is part of a nucleus. (F) Our implementation of DNN successfully segmented various types of microscopy images. Upper row, images; middle row, ground truth; lower row, binary segmentation output. From left to right: nodes of Ranvier in mice teased nerve fibers stained for pan-neurofascin (DS = 87.79%). Scale bar, 15 μm . CHO cells stained for actin (DS = 95.58%). Scale bar, 25 μm . Segmentation of the nuclei in H&E-stained sections of human cancer tissue (DS = 75.83%). Scale bar, 50 μm .

distribution of the $n = 14,281$ nuclei detected within the image in Fig. 2, C and D.

For the whole cultured CHO cells stained for actin, a DS of 94.96% was reached, for the nodes of

Ranvier in murine nerve fibers stained for pan-neurofascin a DS of 87.79% was reached, and for the nuclei in the H&E section a DS of 75.83% was reached (Fig. 2 F).

For samples with a pronounced class imbalance, such as seen for the DAPI cells (nucleus vs. background: 9.6 vs. 90.4%) or the nodes of Ranvier (node vs. background: 1.3 vs. 98.7%), the corresponding PA of 99.17 or 99.60% was even higher. A metric of particular importance for automated imaging was the reliable detection of each individual object. In both DAPI-stained nuclei and Ranvier nodes, 100% of all objects were detected, with 93.67 and 86.67% of individual objects having a DS of at least 75%.

Integration of deep learning allows for fully automated acquisition of high-content super-resolution data

Next, we designed an intuitive, user-friendly software toolkit that makes use of trained neural networks for a fully automated acquisition of super-resolution dSTORM data. Our software guides the microscope to scan a pre-defined large area of the sample, performs segmentation on the entire image using the deep learning models, translates the segmentation results into meaningful dSTORM imaging positions, and acquires dSTORM images at these specific positions (Fig. 3 A).

This can dramatically improve efficiency, for example, using our approach to image the 14,218 nuclei shown in Fig. 2 C at their individual locations, rather than tiling the entire sample, reduces the total number of images required from 194,002 to just 14,218. This represents a 13.6-fold reduction when using a $25 \times 25 \mu\text{m}$ tile size.

First, we demonstrate that super-resolution microscopy is possible even in dense or large samples using object localization by deep learning. To show that the microscope is able to perform dSTORM imaging autonomously, we tested it on several types of specimens with different shapes and properties (Fig. 3). In all experiments, the user only needed to position the sample, after which up to hundreds of images were autonomously acquired, depending on the sample type and experimental conditions. First, to visualize the cytoskeleton formed by β II-spectrin rings in neural axons with super-resolution microscopy, we employed the multicolor capabilities of the software which allows the use of separate colors for object identification and dSTORM imaging. Since β II-spectrin is present in most cultured cells and is not specific to neural axons, single staining might not provide sufficient specificity. To address this and validate the effectiveness of our method in dense samples, we applied double immunofluorescence staining, neurofilament to specifically identify axons, and β II-spectrin to visualize the cytoskeleton with dSTORM. Second, we conducted a large high-content scan (Fig. 3 B), followed by image segmentation (Fig. 3 C, green) and localization of imaging positions, us-

ing neurofilament, a reliable neuron marker, in one color channel. Subsequently, dSTORM imaging was performed on a separate channel stained for β II-spectrin at the identified positions. Using this approach, we were able to resolve the subdiffractional periodic organization of the β II-spectrin rings that conventional imaging methods are unable to resolve (Fig. 3 D).

Next, we tested a different, small ring-like structure. We used SpheroRulers and achieved a reliable identification and revelation of their ring-like appearance in two-dimensional imaging, as opposed to the filled-circle appearance observed in conventional wide-field imaging (Fig. 3 E). For objects larger than the microscope's field of view, such as the CHO cells in our study, random sampling and stitching options for dSTORM were implemented. The dSTORM images shown in Fig. 3 F display images taken at such random sampled positions within a segmented cell cluster. By incorporating deep learning, we fully automated the acquisition of dSTORM images, which revealed subdiffraction-limit structures in the samples, demonstrating capabilities that are not achievable with conventional resolution methods.

Automated STORM achieves similar resolution and high accuracy compared with conventional dSTORM

Next, we assessed the resolution achieved by our method and compared the measurements with previously reported results to validate accuracy.

First, we calculated the average resolution achieved during the automated acquisition of dSTORM images of SpheroRulers, a widely available testing sample. Here, we calculated the resolution using Fourier-ring correlation across all images acquired with automated dSTORM in a single experiment, 63 images in total, and achieved an average resolution of $34.14 \pm 8.97 \text{ nm}$, thus a super-resolution comparable with conventional dSTORM.

To validate the acquired images in terms of accuracy, we measured the periodicity of the periodically organized β II-spectrin rings in neural axons using the previous gold standard of autocorrelation (5), by manually selecting small ROIs in the axons (Fig. 4 B). Here, we measured a mean value of 190 nm (IQR: 180–200 nm) retrieved from $n = 1017$ peak-to-peak distances, corresponding to previously published data (50) and thus showing that the methods achieve highly accurate results.

The software as an open-source tool kit can be extended with advanced image analysis routines

The introduction of automated high-content data acquisition presents the challenge of managing and

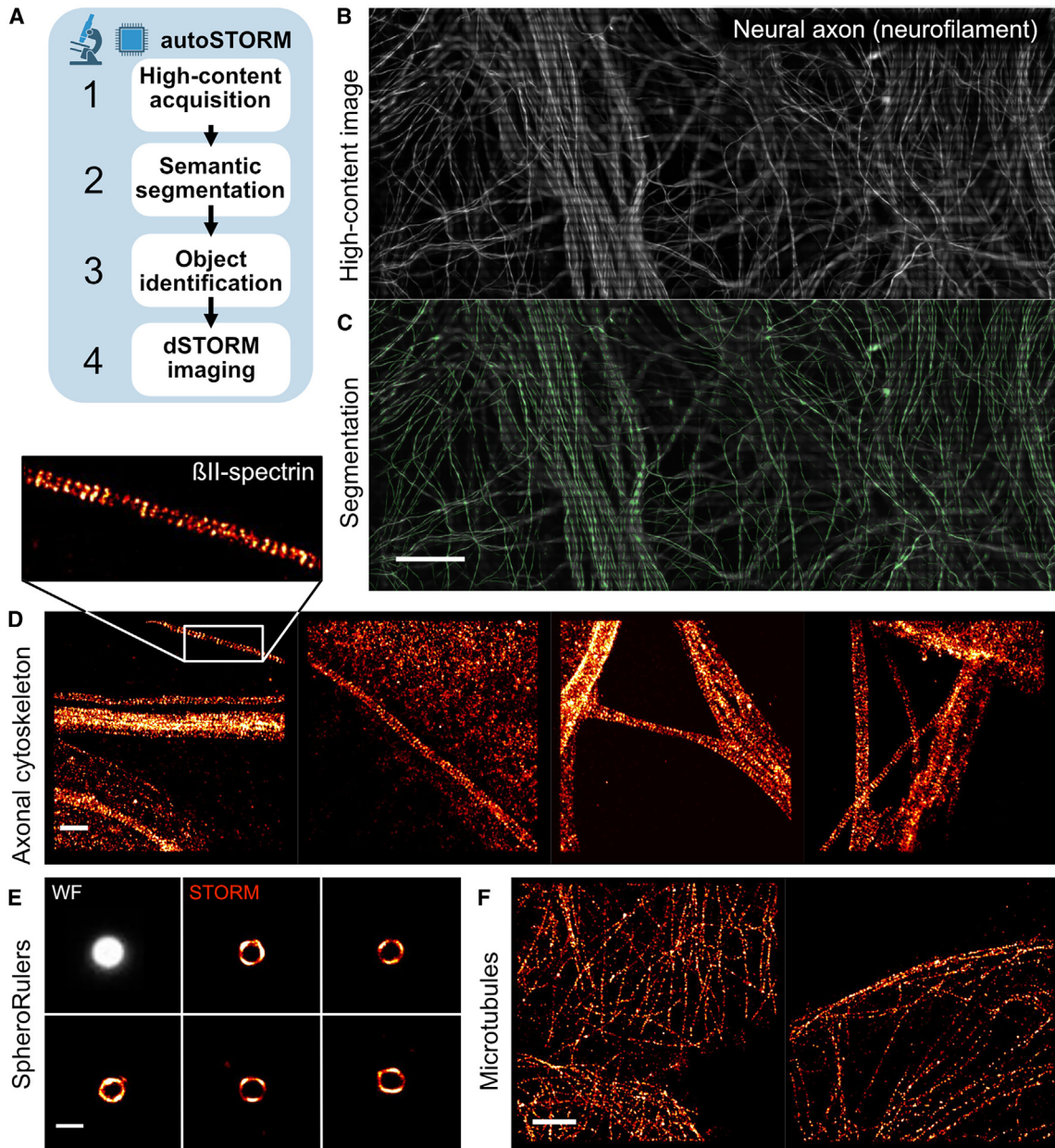


FIGURE 3 Automated STORM acquisition for high-content dSTORM data. By integrating deep learning into the acquisition routine of super-resolution imaging, super-resolved images can be acquired completely autonomously. (A) Acquisition followed an automatic four-step protocol: high-content image acquisition, followed by semantic image segmentation, followed by object identification and lastly dSTORM imaging. (B and C) For imaging of β II-spectrin in neural axons, the axons were identified in separate color channel stained for neurofilament. (B) The high-content image shows plenty of neural axons in a DRG-neuron culture. Scale bar, 100 μ m. (C) The DNN was able to segment these axons for later automated imaging (green overlay). (D) Four out of 256 autonomously acquired dSTORM images of β II-spectrin at the identified axons are shown. Super-resolution images reveal the periodic organization of the cytoskeleton from one experiment. (E) Autonomously acquired dSTORM images of dye-coated microspheres (SpheroRulers) visualize the resolution gain in comparison to a standard wide-field image (upper left). (F) Two autonomously acquired dSTORM images of microtubules in CHO are shown, which were acquired at random positions within a segmented cell cluster in high-content imaging.

analyzing large, complex data sets, which is why our software is open-source and can be easily extended with additional image reconstruction and analysis tools. Here, we show one exemplary extension tool for the analysis of periodic structures without manual

ROI selection that outperforms the previous gold standard shown above.

Instead of image-based autocorrelation, which is the gold standard for determining periodic structures (5), we created an algorithm that is directly based on

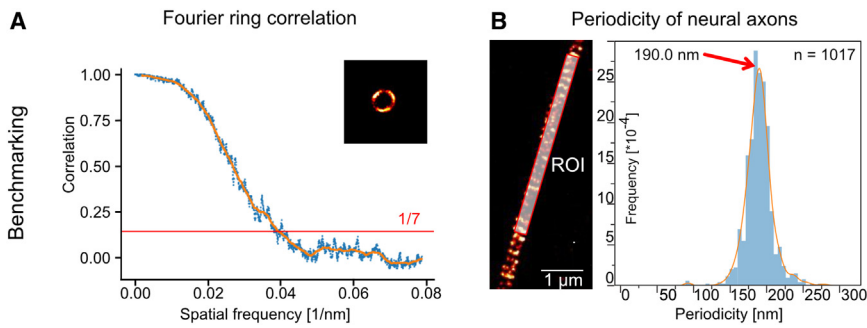


FIGURE 4 Automatic acquisition reaches a high resolution and gives accurate results. (A) Fourier ring correlation was performed on SpheroRulers to calculate average resolution. Here, one exemplary correlation plot is shown. As a threshold for resolution estimation, $1/7$ was used (red). (B) To check the accuracy of our software we measured the experimental periodicity of neural axons to compare it with prescribed values using autocorrelation. Left: manual chosen ROI is shown as an overlay over a dSTORM image of a neural axon. Histogram of the retrieved peak-to-peak distances in autocorrelations from one experiment shows a median periodicity of 190 nm (IQR: 180–200 m), $n = 1017$ spacings.

the localization data calculating the periodicity from the pairwise distances between individual emitters, as multiples of the periodicity should appear more often than other distances. An exemplary dSTORM image and all pairwise distances of one emitter are shown in Fig. 5, A and B. By applying a spline fit to the axons, we enhanced the prominence of the peaks

representing true periodicity, as shown by the red arrows in Fig. 5 C. Subsequently, we extracted the periodicity by correlating the data with adapted sums of normal distributions. Last, we benchmarked the routine on identical simulations against the previous gold standard autocorrelation. First, we checked if different periodicities were measured

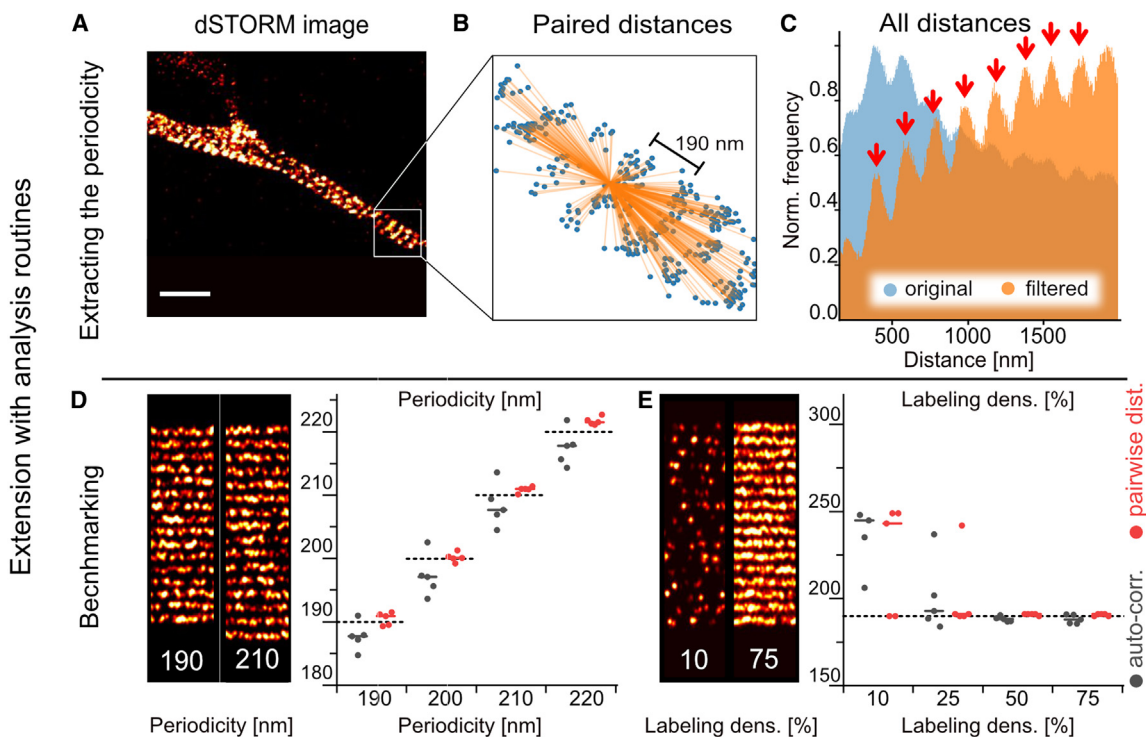


FIGURE 5 Extending automated imaging with complex image analysis of neural axons. For faster extraction of axonal periodicities, we developed an extension, which is not dependent on ROI selections or straight regions. (A) dSTORM image of β II-spectrin in neural axons (B) Scatterplot of all detected emitters in a cropped region of (A) (blue), overlaid with all pairwise distances of one emitter (orange). (C) Histogram of all pairwise distances of all emitters of image (A) (blue). Filtered by a spline fit to the course of the axon pronounces the peaks, which represent the periodic arrangement of the emitters (orange). The peaks are marked with red arrows. (D) Simulated axons with different periodicities can be deciphered with high significance (autocorr. vs. pairwise dist.): $d = 190$ nm, means = 187.7 vs. 190.5 nm; $d = 200$ nm, means = 197.2 vs. 200.1 nm; $d = 210$ nm, means = 208.4 vs. 210.9 nm; $d = 220$ nm, means = 217.5 vs. 221.7 nm; $d = 230$ nm, means = 229.1 vs. 230.3 nm. (E) The periodicity can be retrieved with high accuracy even in challenging conditions such as low labeling densities (ld) (autocorr. vs. pairwise dist.): ld = 10% means = 256.7 vs. 224.2 nm; ld = 25%, means = 200.7 vs. 200.8 nm; ld = 50%, means = 188.2 vs. 190.8 nm; ld = 75%, means = 188.2 vs. 190.6 nm; ld = 100%, means = 187.1 vs. 190.6 nm.

correctly (Fig. 5 D). Here, the algorithm measured the periodicity correctly in all cases with a mean-squared error of just 1.3 nm, which was significantly lower than measured with autocorrelation (1.3 vs. 10.7 nm, $p < 0.001$). The algorithm also distinguished the different periodicities from each other ($p < 0.0001$). The pairwise distance algorithm was also superior in continuously reducing the labeling density, where it correctly measured two out of five periodicities even with a labeling density as low as 10% (Fig. 5 E).

DISCUSSION

This work introduces a user-friendly software toolkit for the automated acquisition of super-resolution dSTORM data. Our implementation successfully segments a range of microscopy images, delivering high segmentation accuracy. Furthermore, we show that these deep learning segmentation algorithms can be used to acquire high-quality high-content dSTORM data, which can be integrated with analysis tools that outperform existing standard methods.

While dSTORM offers a superior resolution of around 50–20 nm compared with about 250 nm for standard wide-field microscopy (3,12,51), it is time-consuming for two key reasons. First, capturing each image can take minutes to hours. Second, identifying new imaging positions is difficult due to fluorophore bleaching or off-switching near the imaging area (52). These challenges limit the use of dSTORM for large samples and high-content screens, which are in research areas such as cancer cell vulnerability studies or histopathological studies (15–18). In our approach, we achieved super-resolution, while improving the imaging process efficiency and drastically reducing user hands-on time. By performing one high-content screen and identifying impositions upfront, we streamlined the imaging process, eliminating the need to search for new positions. This effect is particularly beneficial when objects of interest are rare and easily missed. In addition, having a high-content image as a reference makes the process more systematic and facilitates follow-up analysis.

In summary, automated dSTORM acquisition facilitates the efficient and systematic collection of high-content super-resolution images with minimal user involvement. Although each dSTORM image in our software still took several minutes to achieve high resolution, this posed no significant inconvenience as the user intervention was only necessary during the initial setup. The microscope could then operate autonomously, allowing imaging to proceed during nights and weekends.

Higher-throughput super-resolution could potentially be achieved by modifying the image acquisition

process itself. However, while such techniques can expedite individual acquisition, they often come at the cost of reduced resolution and may introduce additional technical or computational complexities (53–56). In our approach, the resolution could theoretically also be affected by the prolonged use of a single imaging buffer and by preselecting imaging positions before STORM imaging, which may result in imaging already prebleached regions due to scattered light. While both effects could reduce fluorophore performance, we still achieved super-resolution. In summary, automated dSTORM acquisition facilitates the efficient and systematic collection of high-content super-resolution images with minimal user involvement, striking a balance between throughput and image quality.

Open source is crucial for ensuring reproducibility in scientific research, as it allows others to access, verify, and build upon existing work. The software described here was developed and tested on a standard wide-field microscope with particular additional components. However, it was based on two platforms (pylablib and micromanager) that support a wide range of different devices and components (40–42). This allows for straightforward adaptation of the setup to the requirements of individual research groups or cost-effective construction of a custom setup. Our software was designed as an open-source toolkit that can be modularly extended, thereby enabling users to readily customize and extend its functionality to align with specific research requirements. In our case, we developed a Python extension to measure axonal periodicity, which proved to be highly accurate. In addition to extension also key parts of the software could be exchanged. For even faster acquisition but at the cost of its resolution, the STORM acquisition could, e.g., be exchanged by super-resolution radial fluctuations (57). In summary, we present an open-source toolkit for automated acquisition of super-resolution data, that can be extended to fit different goals.

With the success of super-resolution approaches, bias in data analysis (58,59) remains a challenge. Bias and reproducibility are frequently discussed in deep learning, as neural networks rely entirely on their training data, which may not always be free of bias (14,19,60). This is important to consider when selecting training data for fully automated imaging of super-resolution data, as it has to be an accurate representation to make sure all desired objects are detected and imaged (61). Conversely, our methodology for the automated acquisition of dSTORM data removes human bias in object selection. Once a network has been trained and evaluated by experts, it consistently identifies the same objects, regardless of the

user, which ensures that the same objects are imaged, e.g., when multiple researchers are working together or in a multicenter context. It also allows for nonexperts to perform the dSTORM imaging with expert-level object selection and therewith offers interesting options for diagnostic routines.

In conclusion, this work introduces a user-friendly DNN solution for the segmentation of microscopy images, paired with a toolkit for the automated acquisition of dSTORM super-resolution data. The toolkit is freely available, customizable, and scalable, enabling adaptation to data sets of varying sizes or diverse imaging setups. In conclusion, this work introduces an easy-to-use DNN solution for the segmentation of microscopy images, paired with a toolkit for automated imaging of dSTORM super-resolution data. The toolkit is freely available for others to modify, customizable, and scalable to be adapted for biomedical data of various sizes or diverse imaging setups. By integrating super-resolution microscopy into high-content analysis workflows for large samples, this approach has the potential to make imaging even more accessible, supporting a wide range of state-of-the-art studies across multiple research fields.

DATA AND CODE AVAILABILITY

The source code and jupyter notebooks for training and application of neural networks, automated dSTORM acquisition, image reconstruction, and data analysis including exemplary testing data can be retrieved from Zenodo: <https://doi.org/10.5281/zenodo.14690875>. Further raw data including dSTORM data and simulations will be available upon request by any qualified researcher.

ACKNOWLEDGMENTS

The study was supported by a grant of the Interdisciplinary Center of Clinical Research (IZKF) of the Medical Faculty of Würzburg to K.D. and K.G.H (grant nos. F-N-439 and Z-12). L.A. and K.D. hold research fellowships by the Interdisciplinary Center of Clinical Research (IZKF) of the Medical Faculty of Würzburg. J.T.L. was supported by a scholarship of the Graduate School of Life Sciences (GSLS) of the Julius-Maximilians-Universität Würzburg (JMU). We thank Kerstin Jansen and Barbara Reuter for excellent technical assistance. We thank Vinicius da Cruz Neris Geßner for discussions, preparing the SpheroRulers and providing dSTORM reagents.

AUTHOR CONTRIBUTIONS

Conceptualization, J.T.L. and K.G.; data curation, J.T.L. and L.A.; formal analysis, J.T.L.; methodology, J.T.L., L.A., K.D., and K.G.; software, J.T.L.; visualization, J.T.L.; writing – original draft, J.T.L.; writing – review & editing, L.A., K.D., and K.G.; funding acquisition, K.D. and K.G.; project administration, K.D. and K.G.; resources, K.D. and K.G.; supervision, K.D. and K.G.

DECLARATION OF INTERESTS

The authors have declared that no conflict of interest exists.

REFERENCES

1. Schermelleh, L., A. Ferrand, ..., G. P. C. Drummen. 2019. Super-resolution microscopy demystified. *Nat. Cell Biol.* 21:72–84.
2. Sauer, M., and M. Heilemann. 2017. Single-Molecule Localization Microscopy in Eukaryotes. *Chem. Rev.* 117:7478–7509.
3. van de Linde, S., A. Löschberger, ..., M. Sauer. 2011. Direct stochastic optical reconstruction microscopy with standard fluorescent probes. *Nat. Protoc.* 6:991–1009.
4. Vicidomini, G., P. Bianchini, and A. Diaspro. 2018. STED super-resolved microscopy. *Nat. Methods.* 15:173–182.
5. Appeltshauer, L., J. Linke, ..., K. G. Heinze. 2023. Super-resolution imaging pinpoints the periodic ultrastructure at the human node of Ranvier and its disruption in patients with polyneuropathy. *Neurobiol. Dis.* 182:106139.
6. D'Este, E., D. Kamin, ..., S. W. Hell. 2017. Ultrastructural anatomy of nodes of Ranvier in the peripheral nervous system as revealed by STED microscopy. *Proc. Natl. Acad. Sci. USA.* 114:E191–E199.
7. Xu, K., G. Zhong, and X. Zhuang. 2013. Actin, spectrin, and associated proteins form a periodic cytoskeletal structure in axons. *Science.* 339:452–456.
8. Crossman, D. J., P. N. Ruygrok, ..., C. Soeller. 2015. Next-generation endomyocardial biopsy: the potential of confocal and super-resolution microscopy. *Heart Fail. Rev.* 20:203–214.
9. Garcia, E., J. Lightley, ..., P. M. French. 2021. Application of direct stochastic optical reconstruction microscopy (dSTORM) to the histological analysis of human glomerular disease. *J. Pathol. Clin. Res.* 7:438–445.
10. Whelan, D. R., T. Holm, ..., T. D. M. Bell. 2014. Focus on Super-Resolution Imaging with Direct Stochastic Optical Reconstruction Microscopy (dSTORM). *Aust. J. Chem.* 67:179–183.
11. Heilemann, M., S. van de Linde, ..., M. Sauer. 2008. Subdiffraction-resolution fluorescence imaging with conventional fluorescent probes. *Angew Chem. Int. Ed. Engl.* 47:6172–6176.
12. Lelek, M., M. T. Gyparaki, ..., C. Zimmer. 2021. Single-molecule localization microscopy. *Nat. Rev. Methods Primers.* 1:39.
13. Diekmann, R., M. Kahnwald, ..., J. Ries. 2020. Optimizing imaging speed and excitation intensity for single-molecule localization microscopy. *Nat. Methods.* 17:909–912.
14. Renard, F., S. Guedria, ..., N. Vuillerme. 2020. Variability and reproducibility in deep learning for medical image segmentation. *Sci. Rep.* 10:13724.
15. Mulrane, L., E. Rexhepaj, ..., W. M. Gallagher. 2008. Automated image analysis in histopathology: a valuable tool in medical diagnostics. *Expert Rev. Mol. Diagn.* 8:707–725.
16. McGee, J. P., P. Su, ..., N. L. Kelleher. 2023. Automated imaging and identification of proteoforms directly from ovarian cancer tissue. *Nat. Commun.* 14:6478.
17. Shariff, A., J. Kangas, ..., R. F. Murphy. 2010. Automated image analysis for high-content screening and analysis. *J. Biomol. Screen.* 15:726–734.
18. Boutros, M., F. Heigwer, and C. Laufer. 2015. Microscopy-based high-content screening. *Cell.* 163:1314–1325.
19. Griebel, M., D. Segebarth, ..., C. M. Flath. 2023. Deep learning-enabled segmentation of ambiguous bioimages with deep-flash2. *Nat. Commun.* 14:1679.
20. Isensee, F., P. F. Jaeger, ..., K. H. Maier-Hein. 2021. nnU-Net: a self-configuring method for deep learning-based biomedical image segmentation. *Nat. Methods.* 18:203–211.

21. Falk, T., D. Mai, ..., O. Ronneberger. 2019. U-Net: deep learning for cell counting, detection, and morphometry. *Nat. Methods*. 16:67–70.
22. Abdollahzadeh, A., I. Belevich, ..., J. Tohka. 2021. DeepACSON automated segmentation of white matter in 3D electron microscopy. *Commun. Biol.* 4:179.
23. Bannon, D., E. Moen, ..., D. Van Valen. 2021. DeepCell Kiosk: scaling deep learning-enabled cellular image analysis with Kubernetes. *Nat. Methods*. 18:43–45.
24. Stringer, C., T. Wang, ..., M. Pachitariu. 2021. Cellpose: a generalist algorithm for cellular segmentation. *Nat. Methods*. 18:100–106.
25. Fox, Z. R., S. Fletcher, ..., G. Batt. 2022. Enabling reactive microscopy with MicroMator. *Nat. Commun.* 13:2199.
26. André, O., J. Kumra Ahnlide, ..., P. Nordenfelt. 2023. Data-driven microscopy allows for automated context-specific acquisition of high-fidelity image data. *Cell Rep. Methods*. 3:100419.
27. Chiron, L., M. Le Bec, ..., P. Hersen. 2022. CyberSco.Py an open-source software for event-based, conditional microscopy. *Sci. Rep.* 12:11579.
28. Mahecic, D., W. L. Stepp, ..., S. Manley. 2022. Event-driven acquisition for content-enriched microscopy. *Nat. Methods*. 19:1262–1267.
29. Chen, L.-C., G. Papandreou, ..., H. Adam. 2017. Rethinking atrous convolution for semantic image segmentation. Preprint at arXiv. <https://doi.org/10.48550/arXiv:170605587>.
30. Paszke, A., S. Gross, ..., S. Chintala. 2019. Pytorch: An imperative style, high-performance deep learning library. *In Advances in neural information processing systems*, 32.
31. Kingma, D. P., and J. Ba. 2014. Adam: A method for stochastic optimization. Preprint at arXiv. <https://doi.org/10.48550/arXiv:14126980>.
32. Hunter, J. D. 2007. Matplotlib: A 2D graphics environment. *Comput. Sci. Eng.* 9:90–95.
33. Kluyver, T., and B. Ragan-Kelley, Jupyter Development Team. Jupyter Notebooks—a publishing format for reproducible computational workflows. *Press, Positioning and Power in Academic Publishing: Players, Agents and Agendas*. p. 87 [Accessed 902016 2016].
34. Dice, L. R. 1945. Measures of the amount of ecologic association between species. *Ecology*. 26:297–302.
35. Ovesný, M., P. Křížek, ..., G. M. Hagen. 2014. ThunderSTORM: a comprehensive ImageJ plug-in for PALM and STORM data analysis and super-resolution imaging. *Bioinformatics*. 30:2389–2390.
36. Schindelin, J., I. Arganda-Carreras, ..., A. Cardona. 2012. Fiji: an open-source platform for biological-image analysis. *Nat. Methods*. 9:676–682.
37. Holden, S. J., S. Uphoff, and A. N. Kapanidis. 2011. DAOSTORM: an algorithm for high-density super-resolution microscopy. *Nat. Methods*. 8:279–280.
38. Babcock, H. 2023. storm-analysis. 2.2 ed., Cambridge MA, U.S.A., <https://github.com/ZhuangLab/storm-analysis/releases/tag/v2.2>.
39. Nieuwenhuizen, R. P. J., K. A. Lidke, ..., B. Rieger. 2013. Measuring image resolution in optical nanoscopy. *Nat. Methods*. 10:557–562.
40. Edelstein, A. D., M. A. Tsuchida, ..., N. Stuurman. 2014. Advanced methods of microscope control using μ Manager software. *J. Biol. Methods*. 1:e10.
41. Pinkard, H., N. Stuurman, ..., L. Waller. 2021. Pycro-Manager: open-source software for customized and reproducible microscope control. *Nat. Methods*. 18:226–228.
42. Shkarin, A. 2022. PyLabLib: Python package for device control and experiment automation. 1.4.0 ed, <https://github.com/AlexShkarin/pyLabLib>.
43. Van der Walt, S., J. L. Schönberger, ..., T. Yu. 2014. scikit-image: image processing in Python. *PeerJ*. 2:e453.
44. Virtanen, P., R. Gommers, ..., SciPy 1.0 Contributors. 2020. SciPy 1.0: fundamental algorithms for scientific computing in Python. *Nat. Methods*. 17:261–272.
45. Venkataramani, V., F. Herrmannsdörfer, ..., T. Kuner. 2016. SuReSim: simulating localization microscopy experiments from ground truth models. *Nat. Methods*. 13:319–321.
46. Taveggia, C., and A. Bolino. 2018. DRG Neuron/Schwann Cells Myelinating Cocultures. *Methods Mol. Biol.* 1791:115–129.
47. Appeltshauer, L., H. Junghof, ..., K. Doppler. 2023. Anti-pan-neurofascin antibodies induce subclass-related complement activation and nodo-paranodal damage. *Brain*. 146:1932–1949.
48. Kumar, N., R. Verma, ..., A. Sethi. 2020. A Multi-Organ Nucleus Segmentation Challenge. *IEEE Trans. Med. Imag.* 39:1380–1391.
49. Kumar, N., R. Verma, ..., A. Sethi. 2017. A dataset and a technique for generalized nuclear segmentation for computational pathology. *IEEE Trans. Med. Imag.* 36:1550–1560.
50. Leterrier, C., P. Dubey, and S. Roy. 2017. The nano-architecture of the axonal cytoskeleton. *Nat. Rev. Neurosci.* 18:713–726.
51. Born, M., and E. Wolf. 2013. Principles of optics: electromagnetic theory of propagation, interference and diffraction of light. Elsevier.
52. Xu, J., H. Ma, and Y. Liu. 2017. Stochastic Optical Reconstruction Microscopy (STORM). *Curr. Protoc. Cytom.* 81:12.46.1–12.46.27.
53. Torres-García, E., R. Pinto-Cámara, ..., A. Guerrero. 2022. Extending resolution within a single imaging frame. *Nat. Commun.* 13:7452.
54. Li, Y., M. Tingey, ..., W. Yang. 2021. High-speed super-resolution imaging of rotationally symmetric structures using SPEED microscopy and 2D-to-3D transformation. *Nat. Protoc.* 16:532–560.
55. Zhao, W., S. Zhao, ..., L. Chen. 2022. Sparse deconvolution improves the resolution of live-cell super-resolution fluorescence microscopy. *Nat. Biotechnol.* 40:606–617.
56. Gustafsson, N., S. Culley, ..., R. Henriques. 2016. Fast live-cell conventional fluorophore nanoscopy with ImageJ through super-resolution radial fluctuations. *Nat. Commun.* 7:12471.
57. Culley, S., K. L. Tosheva, ..., R. Henriques. 2018. SRRF: Universal live-cell super-resolution microscopy. *Int. J. Biochem. Cell Biol.* 101:74–79.
58. Lee, R. M., L. R. Eisenman, ..., T.-L. Chew. 2024. Believing is seeing – the deceptive influence of bias in quantitative microscopy. *J. Cell Sci.* 137:jcs261567.
59. Jost, A. P.-T., and J. C. Waters. 2019. Designing a rigorous microscopy experiment: Validating methods and avoiding bias. *J. Cell Biol.* 218:1452–1466.
60. Laine, R. F., I. Arganda-Carreras, ..., G. Jacquemet. 2021. Avoiding a replication crisis in deep-learning-based bioimage analysis. *Nat. Methods*. 18:1136–1144.
61. Tommasi, T., N. Patricia, ..., T. Tuytelaars. 2017. A Deeper Look at Dataset Bias. *In Domain Adaptation in Computer Vision Applications*. G. Csurka, ed Springer International Publishing, Cham, pp. 37–55.